The Influence of the Cellular Instability on Lead Shock Evolution in Weakly Unstable Detonation

Scott I. Jackson*

Shock and Detonation Physics Group
Los Alamos National Laboratory, Los Alamos, NM 87545 USA

Mark Short

Shock and Detonation Physics Group
Los Alamos National Laboratory, Los Alamos, NM 87545 USA

Abstract

The evolution of the normal detonation shock velocity (D_n) with local shock curvature (κ) is experimentally and numerically examined along entire evolving fronts of a weakly unstable cellular detonation instability cycle with the intention of extending the understanding of cellular evolution dynamics. As expected, a single velocity–curvature relation is not recovered due to the unsteady evolution of the cell. However, geometric features of the D_n–κ evolution during a cell cycle reveal some new details of the mechanisms driving cellular detonation. On the cell centerline, the local shock velocity and curvature monotonically decrease throughout the cellular cycle. Off centerline, a larger range of wavefront curvature was exhibited in expanding cells as compared to shrinking ones, indicating that most curvature variation in a detonation cell occurs near the Mach stem. In normal shock velocity–curvature space, the cell dynamics can be mapped to three features that are characteristic of (feature 1) a detonation with a spatially short reaction zone, (feature 2) a transitional regime of shock and reaction zone decoupling, and (feature 3) a diffracting inert blast wave. New, growing cells predominately exhibited features 1 and 2, while decaying cells only exhibited feature 3. The portions of all profiles with normal velocities below the Chapman–Jouguet velocity were

*Corresponding author

Email addresses: `sjackson@lanl.gov` (Scott I. Jackson), `short1@lanl.gov` (Mark Short)

URL: `public.lanl.gov/sjackson` (Scott I. Jackson)

characteristic of inert blast propagation, indicating the possibility that exceeding this velocity may be a necessary condition for the existence of shock and reaction zone coupling. In this inert blast regime, D_n and κ vary spatially across the wave front so each segment is not geometrically cylindrical, but when accumulated, the D_n–κ data map out a straight line, indicating elements of self-similar flow for each stage in the cell cycle.

Keywords: detonation, cellular instability, curvature, Detonation Shock Dynamics

1. Introduction

Cellular instabilities are observed to occur for self-sustained detonation propagation in gaseous explosives. These instabilities are driven by shock waves that propagate normal to the detonation shock surface in a Mach-stem configuration. Experimental observations have indicated that periodic interactions of these transverse waves are necessary for unsupported detonation propagation [1].

The instability cycle starts when transverse wave collisions locally increase the flow temperature, overdriving the lead shock, shortening the reaction zone, and tightly coupling the chemical reaction zone to the shock (Fig. 1). The lead shock strength decays as it propagates and the transverse waves move further apart, resulting in gradual decoupling of the reaction zone until subsequent transverse wave interactions locally reinvigorate the flow and start the cycle anew.

The presence of multiple waves causes the surface of the lead shock to pulsate longitudinally as alternating regions undergo different phases of the instability. In practice, a myriad of transverse wave modes are possible depending on the system geometry and explosive thermicity. For example, detonations near failure will support only a single transverse wave, termed single-head spin after the helical path traced by the wavefront in a cylindrical confiner. Mixtures with a comparatively shorter reaction zone length will contain multiple transverse waves [2].

The cellular cycle derives its name from the shape of the triple-point (of the lead shock, Mach stem and transverse wave intersection) tracks mapped on any solid confining walls in the presence of multiple transverse waves. Regular repeating track patterns are indicative of weakly unstable behavior, while highly irregular patterns are characteristic of highly unstable detonation [2]. The characteristic width of these patterns is termed the cell width λ and provides a measure of the mixture sensitivity to detonation. Decreased λ denotes more rapid chemical reaction rates and increased mixture sensitivity. The level of instability is thought to be driven by a mixture's chemical and gas-dynamic properties, as reviewed in Refs. [2, 3].

Early efforts [4–7] attempted to characterize the cellular cycle and reaction kinetics by measuring variations in the lead shock velocity with distance along the cell centerline via schlieren framing imaging. Early in the cycle, the centerline shock velocity was seen to be significantly overdriven relative to the Chapman-Jouguet velocity D_{CJ}, but rapidly and monotically decreased over the cell length in similar fashion to a decaying inert shock wave [6]. The dynamics of off-centerline wavefront regions were not quantitatively examined and no comparisons were drawn to prior condensed-phase explosive research that developed relations between detonation velocity and shock front curvature [8–10].

1.1. The Basics of DSD Theory

Recently, there has been interest in performing more detailed characterization of gaseous detonation wavefronts using concepts derived from Detonation Shock Dynamics (DSD) theory. DSD is a surface propagation concept that replaces the detonation shock and reaction zone with an evolving surface that evolves according to a normal-velocity evolution law [11–13]. In condensed explosives, wavefront curvature κ is assumed to be small relative to the inverse of the length of the detonation reaction zone. It is also assumed that the front shape evolves slowly relative to the time for a particle to pass through the reaction zone. For small κ, the local normal detonation velocity D_n is constant to leading order, with the first correction being a function of shock curvature such that $D_n = f(\kappa)$. This function is referred to as the explosive's velocity–curvature or D_n–κ relationship. Higher-order corrections also exist to account for the influence of time-dependent and transverse flow effects in condensed explosives with large reaction zones and quasi-steady, stable detonations [14].

Significantly, the D_n–κ relationship of a condensed explosive can provide insight into its sensitivity and detonation propagation characteristics. Ideal, insensitive, and nonideal D_n–κ trends for steady high-explosive detonations are shown in Fig. 2. Increasingly nonideal detonations have spatially larger reaction zones and are seen to have a greater depreciation of detonation velocity with wave curvature, support detonation over a more limited curvature span, and thus are more influenced by wave geometry and confinement.

1.2. DSD-Based Approaches to Gaseous Detonation

Application of DSD concepts to gaseous detonations introduces several complications due to the presence of unsteadiness associated with cellular instability. For example, Eckett et al. [15] examined the major contributing factors for direct initiation of spherical detonations, concluding that unsteadiness, rather than curvature, of the decelerating leading shock is the dominant mechanism underlying unsuccessful initiation. In contrast, Short and Sharpe [16] examined the direct initiation of cylindrical detonation reacting via a three-step chain-branching reaction and found that the critical initiation energy for detonations that are hydrodynamically stable along the quasi-steady D_n–κ curve for that mixture could be estimated by the energy required to drive the initial blast shock through the turning point of the quasi-steady D_n–κ curve, validating the critical initiation energy concept of He and Calvin [17] for some stable detonations.

Nevertheless, prior work has attempted to use DSD approaches to examine the initiation and evolution of the cellular structure. Assuming limits of weak curvature and slow temporal variations, Stewart et al. [18] derived an intrinsic surface evolution, comprising a combination of leading and first-order approximations for detonation cell motion. When solved simultaneously, the evolution equation reproduced cells with dynamics apparently similar to those seen in gaseous systems. Yao and Stewart [19], Klein et al. [20], and He and Calvin [17] used numerical and approximate analytic solutions applied to gaseous detonation to predict the existence of a limiting critical κ, beyond which the detonation contained no sonic point. He and Calvin [17] also used this approach to predict minimum initiation energies for gaseous explosives.

Conversely, Nakayama et al. [21] induced global wavefront curvature in excess of that produced by the cellular instability to establish a D_n–κ relationship for ethylene-oxygen mixtures. Significant and quasi-steady global wavefront curvature was generated by detonation propagation around a curved channel and instability effects were mitigated by working with sufficiently sensitive mixtures to allow an excess of 32λ across the channel. Their work described a global and nondimensional D_n–κ relation for the mixtures tested. Such an approach is more in line with DSD's underlying purpose, which uses a surface propagation methodology to reduce the required computational effort (relative to direct numerical simulations using reactive flow models) to generate accurate wave shape and timing predictions while neglecting or homogenizing the smaller-scale details of the wave structure.

1.3. Overview of the Present Study

The purpose of the present article is to analyze the evolution of weakly unstable cellular instabilities for both experimental and numerical detonation. In particular, we study the variation of the normal detonation shock velocity and shock curvature across the whole front surface during the evolution of weakly unstable cellular detonation fronts to gain additional understanding of the dynamics of unsteady cellular evolution. We compare whether the details of the cellular front motion obtained from experiments are consistent with the predictions of a numerical simulation. While less common in practical applications involving hydrocarbon fuels, weakly unstable mixtures are used in the present study to render the our experimental analysis tractable and to allow for highly resolved numerical simulations.

Correspondence to a single $D_n(\kappa)$ relation is not expected due to the unsteady nature of the cellular decay, however understanding the geometric variation of normal detonation with curvature across the front could provide insight into the time-dependent cellular mechanism and the relative sensitivity of gaseous explosive mixtures to geometric effects. We emphasize that we are not claiming that a classical leading-order DSD approach can be used to model detonation cellular dynamics. Classical DSD theory applies to the quasi-steady evolution of a weakly curved, stable detonation; formally asymptotic higher-order corrections which account for (slow) time relaxation effects and small transverse arc-length variations on the evolution of a weakly curved stable detonation have been developed [14, 22, 23]. However, significant rapid time and curvature variations that are believed to occur locally during various stages of the unstable detonation cell cycle preclude such a classical DSD approach to the description of cellular dynamics in general.

2. Two-Dimensional Cellular Instability Data

The instability data in this work is derived from prior experiment and current computation. The specifics of each source are discussed below.

2.1. Experiment

The experimental work of Austin [24] is well-suited for obtaining the variation of D_n and κ across a cellular front in a gaseous detonation. Her experimental facility was a rectangular detonation tube with a narrow channel (NC) cross section that was 152 mm wide $\times$ 18 mm thick $\times$ 4.2 m long. Such a geometry damps out cellular instabilities across the short dimension t = 18 mm for weakly stable mixtures when $t \leq \lambda$ and effectively approximates a two-dimensional cellular instability.

Austin [24] obtained successive shadowgraph images (Fig. 3) of detonation shock shapes through windows embedded in the NC sidewall. Data was recorded on a Beckman and Whitley Model 189 film framing camera with an interframe time of 832 ns, an exposure time of 152 ns, and an image capacity of 25 frames per test. Kodak TMAX 400 black-and-white 35-mm film was used. A single combined schlieren and PLIF (planar laser induced fluorescence) image was also acquired for each test. Additional experimental details are available in Ref. [24].

In the present study, we use shadowgraph images of three separate experiments from Austin [24] to infer the D_n and κ variation for detonation in two separate, weakly unstable, gaseous mixtures: $2H_2$+O_2+17Ar (85% Ar by mole fraction, D_{CJ} = 1.42 mm/μs) and $2H_2$+O_2+12Ar (80%Ar by mole fraction, D_{CJ} = 1.52 mm/μs). Both mixtures were at 0.20 bar initial pressure. Images from the 80%Ar mixture are from experiment numbers NC215 and NC229, while the 85%Ar data is from NC260 in Austin [24]. Films were digitized at 6400 dpi. Two-dimensional detonation shock front shape and image fiducial coordinates were then manually registered for all 25 images from each experiment, resulting in approximately 1200 data points per front.

After digitization and registration, an analytic waveform was fit to each complete cell segment in every image to facilitate evaluation of the local D_n and κ variation. The waveform was similar to that used in Catanach and Hill [25] with additional constants for horizontal (a_x) and vertical (a_z) wave translation and rotation (a_r),

$$\begin{aligned} z(x) &= -a_1 \ln\left[\cos\left[\eta\frac{\pi}{2}\frac{(x-a_x)}{R}\right]\right] \\ &\quad + a_z + a_r\,(x-a_x) \end{aligned} \tag{1}$$

where z is the shock height and x is the transverse width. This wave shape assumes front symmetry about an axis and a monotonic decrease in wave height z away from that axis. For high-explosive rate sticks, R is typically the maximum radius of the charge and normalizes the cosine argument. In this study, R was left as a fitting parameter for each cell along with all a parameters and η. Constraints were imposed such that $0 < \eta < 1$ and $R > w$, where w was each cell's instantaneous width.

Successive front shapes extracted in this fashion for the 85%Ar and 80%Ar mixtures are shown in Figs. 4 and 5 respectively, with channel width and height equivalent to x and z in Eq. 1. Analytic waveforms fit from Eq. 1 are plotted over the black experimental data points, which are of sufficiently high resolution to appear as a continuous curve. Incomplete cell segments at the edge the imaging window were not fit and thus not overlaid with analytic waveforms. Additionally, no fits are overlaid on the experimental data from the first timestep.

The color of each analytic waveform corresponds to the phase ζ of each cell (Fig. 6) as determined by each cell's width w, evolution direction $\frac{dw}{dt}$, and the maximum overall cell width λ_w that was directly observed in each test.

$$\zeta = \begin{cases} \frac{w}{2\lambda_w} & \text{for } \frac{dw}{dt} > 0 \\ 1 - \frac{w}{2\lambda_w} & \text{for } \frac{dw}{dt} \leq 0 \end{cases} \tag{2}$$

With the assumption of a constant detonation cell track angle, parameter ζ is equivalent to the nondimensional cell length. (The track angle is defined as the average angle between the triple point wall intersection trail and the direction of bulk wave motion, which is typically the central tube axis.)

Newly formed cells with ζ near 0 are violet; cells near the middle of their cycle ($\zeta \approx 0.5$) are green; and dying cells ($\zeta \to 1$) are red. The analytic fit correspondence to the experimental data is good, except near the very edge of each cell. The first-order fitting form (Eq. 1) is not able to accurately capture the rapid variations in wavefront curvature in this region. However, these variations are explored in the numerical work.

Parameter λ_w was measured as 38.8 mm, 36.9 mm, and 53.9 mm for tests NC215, NC229, and NC260 respectively. Values of λ_w will be slightly less than or equivalent to the cell size in each test. That said, these cell size data values will vary from those obtained in cylindrical geometries or even in rectangular tubes of different dimensions due to "mode-locking" of the transverse wave to the experimental geometry [26]. During mode-locking, the instability will scale to the confiner geometry and generate an integer number n of cell widths across the channel width ℓ such that

$$\ell = n\,\lambda_w \;\; \text{where } n = 1, 2, 3, \text{etc.} \tag{3}$$

The experimentally measured λ_w values indicate that n = 4 and 3 for the 80%Ar and 85%Ar mixtures, respectively.

The limited observation time imposed by the framing camera record does not allow for substantial evolution of a single cell in the weakly unstable mixtures discussed, but permits simultaneous observation of multiple cells in different phases of evolution. Thus, separate experimental measurements are combined to study the full instability cycle with the assumption that all cells in a test generate a similar D_n and κ evolution across the front.

2.2. D_n and κ Variation Across the Cellular Instability

For the experimental work, the analytic wavefront fits were used to compute the instantaneous axial detonation velocity for a given image i

$$D_i(x,t) = s\frac{z_{(i+2)}(x) - z_{(i-2)}(x)}{4\tau} \tag{4}$$

using the computed shock position shift $z_{(i+2)} - z_{(i-2)}$ (in pixels) between wavefront fits separated by four imaging timesteps τ, and the image scale s. Scale s was approximately 0.030 mm/pixel, but varied for each test as determined by a fiducial square (shown in Fig. 3). Measurement error associated with this process is discussed below. Accounting for the spatial and temporal variations in D is a key difference of this work relative to high-explosive rate sticks efforts, where D is usually steady for a similar rectangular geometry.

Local variations in D_n and κ across the front were then found from

$$D_n = \frac{D}{\sqrt{1+(z')^2}} \tag{5}$$

and

$$\kappa = \frac{z''}{[1+(z')^2]^{3/2}} \tag{6}$$

where $z' = dz/dx$ and $z'' = d^2z/dx^2$. Equation 6 is the curvature for a two-dimensional wavefront and implicitly assumes no curvature on the third axis (dimension t). Thus, a pair of images is required to obtain the D_n variation for each cell, while a single image yields the κ variation. These two measurements are then combined to obtain the D_n and κ curve for *each* cell. In the present work, the choice was made to calculate the average detonation velocity across four imaging timesteps in order to reduce the velocity uncertainty below 1%. Additional details are discussed in the experimental uncertainty section below.

2.2.1. Variation of D_n with ζ

The calculated D_n range for each cell is plotted as a function of ζ in Fig. 7 for NC260 (red) and in Fig. 8 for NC215 (green) and NC229 (black). Each plot contains data points, solid lines, and a dashed line. The data points are the wavefront values along the cell centerline, as have been historically plotted in cellular studies [4–7]. Solid lines denote the span of D_n values (off of the cell centerline as) measured along each front profile. Dashed lines are least-squares fits to the cell centerline points using a $1/\zeta$-functional form that is consistent with previous [4–7] experimental observations,

$$\frac{D_n}{D_{CJ}} = b_1 \frac{1}{\zeta + b_2} + b_3 \tag{7}$$

with specific values listed in Table 1. Parameter ζ is linearly proportional to the axial distance via either the detonation cell track angle or the total cell length. Such a form is also consistent with that of a decaying blast wave, as discussed in Sec. 3.

Table 1: D_n-fit data.

Test	b_1	b_2	b_3
NC215	0.303	0.501	0.592
NC229	0.099	0.233	0.811
NC260	4.19	2.69	-0.494

The D_n data is overdriven ($1.2D_{CJ}$) at the start of the cellular cycle and and subsequently decays down to $0.6D_{CJ}$ with $\frac{dD_n}{d\zeta} < 0$ throughout the cycle. Such a trend agrees with earlier observations [4–7]. Data scatter is apparent in the experimental D_n data. Most is attributed to image digitization and front registration errors. However, the D_n versus ζ centerline data is seen to follow the $1/\zeta$ functional form. Off-centerline D_n-span data (solid lines) also follows the centerline trend, but can vary from the centerline velocities by up to 25%. No correlation is observed for the location of the centerline value on the experimental D_n-span data.

Austin [24] measured the average detonation velocities upstream of the imaging window over a two-meter length in her facility using pressure transducers. She confirmed that sustained detonations were present with average velocity deficits (relative to D_{CJ}) of 7.3% and 12.3% for the 80%Ar and 85%Ar mixtures respectively. (Deficits were expected due to the damping of the cellular instability on the facility's short axis.) Solving for the average centerline detonation velocity across the full cellular cycle via Eq. 7 and Table 1 yields $\frac{D_n}{D_{CJ}}$ = 0.913 (NC215), 0.970 (NC229), 0.813 (NC260). These values correspond to average velocity deficits $(1 - \frac{D_n}{D_{CJ}})$ of 8.7%, 3.0%, and 18.7% for NC215, NC229, and NC260, respectively.

The average velocities derived from the shadowgraph analysis and the pressure transducer measurements are consistent when taking into account (1) the +/-12.5% uncertainty in all length and velocity scales associated with the fiducial squares (discussed in Section 2.3) and (2) the stochastic behavior of large-cell-size detonations over the temporally limited imaging window, which was less than the period of a full cellular cycle for the mixtures considered.

2.2.2. Variation of κ with ζ

Centerline κ values are equivalently fit to the functional form

$$\kappa\lambda_w = c_1 \frac{1}{\zeta + c_2} + c_3 \tag{8}$$

and fit data is listed in Table 2. The κ variation with ζ (Figs. 9 and 10) exhibits a

Table 2: κ-fit data.

Test	c_1	c_2	c_3
NC215	0.862	0.082	-0.674
NC229	0.654	0.077	-0.574
NC260	1.158	0.225	-0.910

strong correlation and separate tests overlay moderately well for higher ζ. Cells with small ζ have nondimensional κ as large as 8. As the cell evolution progresses ($0.2 < \zeta < 0.8$), these values drop significantly, to below unity.

The span of κ values is a strong function of ζ. New and growing cells (small ζ) exhibit very large κ spans, while decaying cells (ζ near 1) have very small spans. Furthermore, a discontinuous drop-off in the span of κ occurs at ζ = 0.5, where the transverse waves at the cell perimeter stop expanding and begin to converge (due to transverse shock collisions). This sudden drop in κ span at the instant that the cell width begins to decrease indicates that *the edges of growing cells exhibit the largest amount of wave curvature across the front.* This effect is illustrated in Fig. 11, which shows the distribution of κ across a cell segment with ζ = 0.44 in NC260. Consistent with this understanding, centerline κ values tend to occupy the lowest κ values present in each cell's κ-span. For $\zeta > 0.5$, κ spans grow very small and these almost only correspond to the centerline value. In these regions, the decayed cell approximates a cylindrical shock geometry (i.e. constant κ along the front).

Near the end of the cell cycle ($0.8 < \zeta \leq 1.0$), κ values anomalously increase. This effect is likely due to difficulty in accurately fitting Eq. 1 to the extremely small and flat decaying segments, which can span only three pixels vertically. (Newly developed cells of similar width cover three times this vertical range, allowing a better fit.)

2.2.3. Variation of D_n with κ

Figures 7–10 can be combined to show the experimental D_n and κ evolution during a complete cell. Figures 12 and 13 plot this relationship versus ζ for NC260 and NC229, respectively. Solid lines correspond to the D_n–κ profiles for each cell segment, with ζ denoted by color. The dashed black lines correspond to the previously described functional-form fits (Eqs. 7 and 8), which are parametrically plotted in D_n–κ space. The compiled measurements form a global trend with cells moving from the upper right of the plots to the lower left as the cell evolves, in a similar trajectory to the decaying blast wave profile shown in Fig. 2 and discussed in Section 4. Early in the cellular cycle (small ζ), a wide range of κ variation is present over a small span of D_n. This D_n–κ trend indicates overdriven cell expansion supported by a spatially narrow reaction zone, similar to D_n–κ trends observed for ideal high explosives (Fig. 2). Late in the cellular cycle (large ζ), the wave's $D_n(\kappa)$ slope is significantly steeper; small changes in κ result in large D_n variations, which are consistent with non-ideal high explosive behavior (spatially long reaction zone, Fig. 2). Intermediate values of ζ show a gradual transition between these two limiting behaviors. Late stage (red) cells exhibit excursions from this trend due to the previously described fitting inaccuracy in κ-space. Equivalent data occurred for NC215, but is not shown.

Thus, analysis of the experimental work both agrees with prior studies and provides increased understanding of the cellular dynamics by analyzing the full perimeter of the cellular wavefront. The local normal detonation velocity trend follows centerline measurements obtained previously [4–7]. Curvature across the front, quantified for the first time in this study, is seen to vary both temporally and spatially. Temporally, the curvature starts at its largest magnitude and overall span for small, overdriven and expanding cells. In contrast, decaying and underdriven cells have the lowest curvature magnitudes and exhibit a very narrow (almost cylindrical) curvature span. Spatially, the lowest amount of curvature occurs at the cell center, while the largest curvature is induced at the edge of expanding cells.

These behaviors are fully consistent with the unsteady nature of the cellular cycle and the presence of multiple cells in different phases across the detonation front. Overdriven cells ($\zeta < 0.5$) diffract into adjacent slower-velocity decayed ones, inducing high κ at the expanding edge of the overdriven cells. In decaying cells ($\zeta \geq 0.5$), the reaction zone gradually decouples from the front, and the unsupported shock front decays cylindrically, as shown in Figs. 9 and 10, into a low-κ, low-D_n state. Additional insight into the D_n–κ behavior is provided via numerical simulation described below.

2.3. Experimental Measurement Uncertainty

Error in the experimental analysis is predominately due to the finite film size and digitization resolution. Misidentification of the front location in an image can result in significant D_n scatter. As an example in the above data, one pixel of wave position error in Δz induces an error in D of 0.6% D_{CJ} when averaging over 4τ. Such sensitivity, coupled with film exposure intensity changes and focal variations from frame-to-frame, can result in significant velocity scatter in D. The κ calculation is more robust as it only requires a good fit of Eq. 1 to a single front segment on a single image frame. However, as discussed, poor fits occur for cells of small transverse width with low curvature due to insufficient number of vertical pixels across the cell.

Finally, variations or misidentification of the fiducial size affects all dimensional measurements present in this work. Up to two small fiducial squares were present on each image (as shown in Fig. 3) and were used to both align and scale the data from pixels to physical units. Fiducial dimensions were measured for each image and then averaged for each experiment. Averaged fiducial values were measured to be 88.4, 127.3, and 135.6 pixels for NC215, NC229, and NC260, respectively. The quoted dimension for each fiducial box was 4-mm square [24], potentially allowing for length variations from 3.50–4.49 mm within the stated significant digit. Fiducial size variations would rescale all quantitative values, but would not affect the trends observed in the experimental data.

3. Numerical Simulation

Given the limited spatial and temporal resolution available from the experimental data, we have also explored the dynamics of normal detonation velocity (D_n) and curvature (κ) variation along the front during the evolution of a detonation cell using high-resolution numerical simulation.

3.1. Computational Scheme

The numerical simulations are based on the non-dimensional reactive Euler equation model for an ideal gas. A one-step reaction model of Arrhenius type was assumed. The equations are

$$\frac{D\rho}{Dt} + \rho(\nabla \cdot \mathbf{u}) = 0, \quad \frac{D\mathbf{u}}{Dt} = -\frac{1}{\rho}\nabla p,$$
$$\frac{De}{Dt} = -\frac{p}{\rho}(\nabla \cdot \mathbf{u}), \quad \frac{D\chi}{Dt} = W, \tag{9}$$

for density ρ, specific internal energy e, velocity $\mathbf{u} = (u, v)$, and reaction progress variable χ. Reference values for the original dimensional variables are the initial reactant density $\tilde{\rho}_0$ (density), initial reactant pressure $\tilde{p}_0$ (pressure), $\sqrt{\tilde{p}_0/\tilde{\rho}_0}$ (velocity) and $\tilde{p}_0/\tilde{\rho}_0$ (specific internal energy), where the use of $\{\tilde{\ }\}$ denotes a dimensional quantity. Consequently $D_n = \tilde{D}_n/\sqrt{\tilde{p}_0/\tilde{\rho}_0}$. The ideal gas equation of state is

$$e = \frac{p}{\rho(\gamma - 1)} - Q\chi, \quad T = p/\rho, \tag{10}$$

for the ratio of specific heats γ and temperature T (scaled with the initial reactant temperature $\tilde{T}_0$). The rate W is

$$W = k(1 - \chi)\exp(-E\rho/p). \tag{11}$$

Using the calculated detonation states corresponding to the $2H_2$–O_2–Ar kinetic mechanism published in Ref. [27], the heat release Q, activation energy E and ratio of specific heats γ, were determined by approximating the calculated one-dimensional Zeldovich-Von Neumann-Döring (ZND) Mach number, post-shock γ and the correct sensitivity of the ignition delay behind the shock obtained with constant volume ignition simulations at the post-shock state. We study the 80%Ar mixture for which the above fitting procedure sets $E = \tilde{E}/\tilde{R}\tilde{T}_0 = 20$, $Q = \tilde{Q}/\tilde{R}\tilde{T}_0 = 10$ and $\gamma = 1.57$, where $\tilde{R}$ is the specific gas constant. Finally, length is scaled with $\tilde{l}_{1/2}$, the distance between the shock and the point where half of the reactant is depleted in the ZND wave, while time is scaled with $\tilde{l}_{1/2}/\sqrt{\tilde{p}_0/\tilde{\rho}_0}$. Consequently, the non-dimensional rate constant $k = 22.719$. Values of the dimensional reference quantities are given in Table 3 based on the initial conditions of the $2H_2$+O_2+80%Ar detonation cell experiment described in Ref. [24].

The solution method uses the two-dimensional shock-fit, shock-attached algorithm and code described by Henrick [28], an extension on the one-dimensional

$\tilde{p}_0$	0.2 bar
$\tilde{\rho}_0$	0.2778 kg/m^3
$\sqrt{\tilde{p}_0/\tilde{\rho}_0}$	268.3 m/s
$\tilde{T}_0$	298 K
$\tilde{D}_{CJ}$	1480.2 m/s
$\tilde{l}_{1/2}$	0.72 mm
$\tilde{l}_{1/2}/\sqrt{\tilde{p}_0/\tilde{\rho}_0}$	2.68μs

Table 3: Dimensional reference values for the numerical simulation [24]. Here $\tilde{l}_{1/2}$ is the distance between the ZND shock and the location of the maximum reaction rate, as opposed to the location where half of the reactant is depleted.

algorithm described by Henrick et al. [29]. The algorithm uses a method of lines approach, with spatial gradients discretized by a fifth-order mapped weighted essentially non-oscillatory scheme and temporal integration via a fifth-order Runge-Kutta method. The shock-attached system allows straightforward determination of the lead shock curvature (using the calculated detonation shock slope) and normal detonation velocity [28]. The two-dimensional shock-fit, shock-attached methodology has previously been used to explore the linear stability and nonlinear dynamics of detonation cell development for the ideal condensed-phase detonation model Short et al. [30].

The calculation is conducted in a two-dimensional channel of width 9 (dimensionally 9 times $\tilde{l}_{1/2}$) with periodic flow conditions at the upper and lower walls. The length of the computational zone is 40, with the lead shock located at $x = 0$ and an outflow boundary at $x = -40$. In the axial direction, the resolution is 0.05 (corresponding to 20 points per half reaction length) and 0.0125 (80 points per half reaction length) across the channel. A discussion of resolution sensitivity for cellular detonations of the two-dimensional shock-fit, shock-attached algorithm [28, 29] is given in Short et al. [30]. These resolution requirements limit the channel width to the above choice, which is smaller than the experimental channel size Austin [24]. The initial conditions consist of a one-dimensional ZND structure imposed across the channel to which a two-dimensional perturbation in the mass fraction variable is added to generate the cellular instability.

3.2. *Computed Cellular Detonation*

Figure 14 shows the evolution of D_n from the initial ZND wave along the channel centerline ($y = 4.5$) with time. Small oscillations in D_n around $D_n = D_{CJ}$ ($D_{CJ} = \tilde{D}_{CJ}/\sqrt{\tilde{p}_0/\tilde{\rho}_0} = 5.517$) grow to a near periodic limit cycle variation corresponding to fully nonlinear cellular detonation. Figure 15 shows instantaneous shapes of the shock loci over one detonation cell cycle duration (from just after the creation of a new cell in the channel near the centerline ($t = 72.0$) to slightly before the disappearance of the cell ($t = 74.0$), and illustrates that a single cell develops for a channel width of 9. The centerline shock loci correspond to $\zeta = 0.01$ ($t = 72$), $\zeta = 0.08$ ($t = 72.25$), $\zeta = 0.016$ ($t = 72.5$), $\zeta = 0.24$ ($t = 72.75$), $\zeta = 0.33$ ($t = 73$), $\zeta = 0.42$ ($t = 73.25$), $\zeta = 0.51$ ($t = 73.5$), $\zeta = 0.57$ ($t = 73.75$), $\zeta = 0.64$ ($t = 74$), $\zeta = 0.73$ ($t = 74.25$), $\zeta = 0.82$ ($t = 74.5$), $\zeta = 0.91$ (($t = 74.75$), $\zeta = 0.97$ ($t = 75$).

For $\zeta < 0.5,$ the interior part of the channel shows the growth of a cell, while for $\zeta \geq 0.5,$ the interior portion of the channel is associated with the cell decay. The normal detonation velocity along the centerline (Fig. 14) shows a monotonic decrease in D_n during the growth and decay of the central cell. The dashed lines show the trajectory of the triple point loci.

Snapshots of the cell pressure and corresponding reaction progress variable in the vicinity of the shock front at $t = 72.5$ ($\zeta = 0.016$), $t = 73.0$ ($\zeta = 0.33$), $t = 73.5$ ($\zeta = 0.51$), $t = 74.0$ ($\zeta = 0.64$) and $t = 74.5$ ($\zeta = 0.82$) are shown in Figs. 16 and 17 respectively. At $t = 72.5,$ a cell is growing outward from the interior into the decaying cells present in the outer portions of the channel. Along the shock front, the pressure appears to increase behind the transverse shocks, before reaching a maximum and decaying toward the channel centerline (see also Fig. 19). Fresh reactant enters the growing cell via both the lead shock and transverse shock leading to the complex variation of the flow field in the vicinity of the Mach stem. However, sufficiently far down the channel, the pressure maximum appears to be reached at the transverse shock. The emergence of a familiar keystone structure is seen in the corresponding reaction progress distribution at $t = 72.5.$ (Fig. 17a). The higher temperature behind the transverse shocks leads to a local acceleration of the reaction rate. The global lead shock curvature associated with the growing cell is greater than the exterior decaying cells. As the cell grows ($t = 73$), the peak of the pressure distribution along the front again occurs at a finite distance behind each transverse shock. The corresponding reaction progress variable plot (Fig. 17b) shows the region of accelerated reaction in the growing interior cell does not extend the width of the cell defined by the location of the transverse shocks. Rather, the extent of the accelerated region is approximately defined by the loci of shock normals along the front of the growing cell. This indicates a potential interlink between variations in the reaction zone structure and shock normal quantities.

At the point of transverse shock collision at the channel edges, there is a region of intense pressure rise near the channel edge (Figs. 16c and 17c). After shock collision, the global curvature of the interior decaying cell decreases, and the reaction zone recedes (Figs. 16d,e and 17d,e). Due to the problem symmetry, the outer sections of the channel correspond to growing cells with structure similar to that observed in Figs. 16a,b and 17a,b.

Figure 18 shows the axial variation of the reaction progress variable χ along the channel center $(y = 4.5)$ at $t = 72.5$, $t = 73.0$, $t = 73.5$, $t = 74.0$ and $t = 74.5$. Only values at numerical cell points are shown to gauge the resolution of the reaction zone structures. Also indicated are the values of one over the centerline shock curvature $(1/\kappa_{CL})$ at the indicated times. At $t = 72.5$, the higher temperature along the growing interior cell leads to a pocket of accelerated reaction which connects downstream to a region of receding reaction created by the earlier decaying cell. As the transverse waves move further away from the centerline, the reaction progress rate decreases and the pocket moves further downstream. The values of one over the centerline shock curvature can be compared to the reaction zone thickness to relate the magnitude of the shock curvature to reaction zone thickness. During the early stages of cell growth (t = 72.5–73.0), these values are comparable. Subsequently (t = 73.5–74.5), $1/\kappa_{CL}$ is greater than the reaction zone thickness. Thus along the centerline, decaying cells have weak shock curvature on the scale of $l_{1/2}$.

Figure 19 shows the distributions of (a) density, (b) axial and (c) transverse flow velocities, (d) pressure and (e) temperature along the lead shock front at times $t = 72.5$, $t = 73.0$, $t = 73.5$, $t = 74.0$ and $t = 74.5$. One of the benefits of the shock-attached, shock-fit algorithm developed in Refs. [28, 29] is the accuracy and ease of the extraction of this data over the interpolation that would be required with the usual shock capturing algorithms. As above, the data points are represented by symbols at each numerical grid point for easier visualization of the location of the numerically captured transverse shock waves. Of particular interest, in light of the discussion of the normal detonation velocity and curvature variation along the front discussed below, is the local structure variation in the vicinity of, and behind, the transverse shock waves. As noted in the growing cell of Fig. 16, the pressure distribution, as well as the temperature and density variation (Fig. 19), show an increase in the state variables after the passage of the transverse shock front, reaching a maxima at a finite distance from the transverse shock, before decaying toward the centerline. In the decaying cell, the pressure, temperature and density variations increase monotonically from the centerline to the transverse shocks.

3.3. Detonation Cell Evolution in the D_n–κ Plane

Figure 20 explores the variation of the instantaneous lead shock shape in the channel, the normal detonation velocity, and the curvature across the lead shock over the duration of a single cell cycle. In Fig. 20a–e, at each time, the shock loci and D_n have been displaced by values indicated in the caption in order to present curves of instantaneous shock position, D_n and κ on one graph. Blue lines indicate shock curvature and green lines are the normal detonation velocity. Red and black lines are the shock loci. Red coloring denotes data from growing cells, while black coloring indicates decaying ones.

Figure 20f–j shows D_n and κ data from the same time steps as Fig. 20a–e on a plot of D_n versus κ. These data are color-matched to the corresponding shock loci. The paired plots allow features in D_n–κ space to be more easily associated with locations on the shock front. In the D_n–κ plots, symbols are used to record values at each numerical grid point to better highlight physical characteristics. Additionally, specific features are identified on each plot and discussed below.

3.3.1. Timestep t = 72.5

At $t = 72.5$, a cell is growing from the channel interior toward the channel edge (Fig. 20a). Between the channel edge and the growing cell, there are two sections of a decaying cell (recall periodic conditions are applied at the channel edges). Figure 20f shows the variation in D_n and κ across the front. In the decaying cells (black lines), the curvature is nearly constant, with a small monotonic increase in D_n from the channel edges to the interior transverse shocks (feature 3, lower branch, in Fig. 20f). This corresponds to near cylindrically symmetric decay of the detonation cell. The structure of the interior growing cell is more complex. In the middle of the cell there is a region of near constant curvature variation associated with a small increase in D_n. This is represented by the cluster of red points in D_n–κ space for $D_n \approx 6.1$. (Subsequent timesteps will show these data to be an upper branch of feature 3.) Approaching the transverse shock from the centerline, a rapid rise in curvature associated with a small increase in D_n is observed. This is followed by a decrease in κ with D_n variation as the transverse shock is reached, forming a "hook-like profile" (feature 2 in Fig. 20f). Finally, immediately adjacent to the transverse shock, κ decays rapidly and changes signs with a slight decrease in D_n (feature 1 in Fig. 20f). Note that only curvatures above -0.5 are shown in Fig. 20.

3.3.2. Negative Curvature

Based on examination of the curvature variation in Fig. 20, we surmise the decaying cell has positive curvature (divergent) everywhere. The transverse shock connects the decaying cell to the growing cell. The growing cell appears to have a region of negative curvature (convergent) behind the transverse shock in the region where the temperature and pressure increase along the front occurs, before transitioning to a positive curvature (divergent). The precise extent of the negative curvatures reached in the convergent region behind the transverse shock is complicated by the role of numerical dissipation in the captured transverse shock.

To illustrate this, Fig. 21 plots again the computed detonation front shape at $t =$ 72.75. The growing central cell is red, the adjacent decaying waves are black, and the cell boundaries are demarcated by green points. The corresponding D_n–κ variation for all computed points is shown in Fig. 22. Numerical dissipation causes the transverse shock to spread over several computational cells (in a formal Euler calculation, the curvature at the shock intersection point would be undefined). From the decaying cell side, the discrete points involving rapid curvature decreases are generated by dissipation in the shock rise. Similarly, for the growing cells, a number of the larger negative curvature cells will be the result of numerical dissipation in the transverse shock. Determining the exact extent of numerical dissipation is difficult. Formal convergence studies are complicated by the nonlinearly unstable evolution. Thus, in Fig. 20, we have chosen to show results for negative curvatures above -0.5 in the growing cells. Finally, we note that the rapid variation and change in sign of κ in the vicinity of transverse shocks would not be detected in the experimental work due to the fitting form (Eq. 1) used.

3.3.3. Subsequent Timesteps

In Figs. 20b and 20g, the interior cell has grown to $\zeta = 0.33$ (at $t = 73.0$), while the adjacent decaying cells have ζ = 0.65. The D_n and κ variation in the decaying cells have almost collapsed to a single point in D_n–κ space (Fig. 20g, feature 3, lower branch), corresponding to near cylindrical decay. Additionally, we note that the curvatures of this feature are sufficiently small to approximate the wave as flat at this stage in the decay cycle. In the growing cell, there is a wider variation in D_n between the centerline and where the hook structure is encountered, leading to a linear D_n–κ variation with positive slope (Fig. 20g, feature 3, upper branch). The hook structure (Fig. 20g, feature 2) that again occurs in the vicinity of the transverse shock has a similar shape to that seen at $t = 72.5$, except a larger (positive) value of curvature is reached, and the hook occurs at lower D_n.

Figures 20c and 20h describe the normal detonation velocity and curvature variation along the lead shock front when the interior cell has reached the channel edge at t = 73.5. This case illustrates the full D_n–κ variation at shock collision. Moving out from the cell centerline, feature 3 displays an approximately steady, monotonic increase in D_n over a narrow range of κ increase. Approaching the transverse shock, feature 3 transitions into the feature 2 hook profile with a rapid change in slope. Feature 2 then smoothly transitions into feature 1 at the Mach stem. Note that a majority of the variation in κ occurs at the cell edge and that the extrema of feature 2 (hook tip) continues to increase in κ and decrease in D_n as the cell evolves from $\zeta = 0 \rightarrow 0.5$. The reader is also urged to observe the gradual lengthening of feature 3 in the growing centerline cell D_n–κ data over timesteps 72.5, 73.0, and 73.5.

The D_n–κ variations for $t = 74$ and $t = 74.5$ are shown in Figs. 20d,e and 20i,j, respectively. The structures are similar to those observed at earlier times, except the decaying cell now occurs in the interior of the channel. Additionally, feature 3, which increased in D_n–κ span with the centerline cell growth from t = 72.5–73.5, can be seen to decay in span with the cell decay.

3.4. Intrepretation of D_n–κ Variation During a Cell Cycle

It appears that the growth and decay of a detonation cell can be collated with three distinct structures in the variation in D_n and κ across the lead shock during a cell cycle. Two of these (features 1 and 3) correspond to approximately linear D_n–κ variation.

Feature 1 was a small slope, large-curvature-span curve for the flow immediately adjacent to the Mach stem. The small slope indicates that the magnitude of the wave curvature in this region is not sufficient to impact the local wave velocity, likely due to to the spatial shortness of the reaction zone. Note that in classical (quasi-steady) DSD theory, this profile is characteristically similar to the "ideal explosive" curve in Fig. 2 that arises due to a spatially small reaction zone. When present (for $0 < \zeta \leq 0.5$), feature 1 contains the peak D_n values in the cell.

Feature 3 exists as a high-slope, narrow-curvature-span line for the oldest and most decayed inner portions of each cell. The high slope may indicate a strong influence of the local curvature on the wave velocity. Such behavior is reminiscent of the curvature influence on velocity that occurs in classical DSD theory for highly nonideal explosive (as a result of their spatially long reaction zones), although nonideal D_n–κ profiles from steady detonations have large negative slopes instead of the positive values exhibited in Fig. 2. In the following section, we also associate feature 3 with a nonreactive, decaying cylindrical blast wave. The span of feature 3 grows with cell growth to a maximum at ζ = 0.5, after which it decreases. The average magnitude of the D_n and κ values present in feature 3 decrease as ζ increases, indicating decreasing wave strength.

Finally, feature 2 or the "hook" structure exists as a transitional structure between the accelerated reaction associated with feature 1 and the decaying detonation associated with feature 3. This feature contains the the peak curvature values for the cell. Significant variation occurs in this region due to the localized growth and decay of pressure and temperature in the vicinity of the transverse shock (Fig. 19).

Growing cells ($\zeta < 0.5$) contain all three structures. In young growing cells ($\zeta < 0.3$), features 1 and 2 are predominant. Feature 3 first appears in growing cells with ζ near 0.3 and grows in size as the cell approaches ζ = 0.5. Decaying cells ($\zeta \geq 0.5$) only contain feature 3 (features 1 and 2 are not present as decaying cells do not contain reactive Mach stems). As the front decays in strength from $0.5 \leq \zeta \leq 1.0$, the span of both D_n and κ decrease.

Thus, the overall evolution trend is as follows: Small cells start with large κ ranges and small-span overdriven D_n values. As the cell grows to ζ of 0.5, the D_n span increases to a maximum and decays slightly in magnitude. The κ span collapses quickly for ζ above 0.5 due to the disappearance of the reactive Mach stem. As the cell decays from $\zeta = 0.5 \rightarrow 1.0$, the magnitude of D_n decreases and the D_n span also rapidly decreases.

Finally, we note simulations have also been conducted on the one-step equivalent of the $2H_2$+O_2+85%Ar mixture in a channel of width 9. A single (mode-locked) cell develops with very similar D_n–κ structures to those observed above. Likely, wider channels would be needed to highlight distinctions in cell structures between the mixtures.

4. $D_n(\kappa)$ for an Expanding, Inert Blast Wave

Figure 23 overlays numerically calculated D_n–κ data from multiple time steps (72.00 to 75.00 in increments of 0.25) constituting the full range of $\zeta = 0 \rightarrow 1$. Two regimes are clearly identified. An overdriven regime (which we define as regions where $D_n > D_{CJ}$) encompasses the large D_n and κ variations near the edges of the growing cells ($\zeta \leq 0.5$), as well as approximately linear D_n–κ regimes corresponding to central portions of the growing cells. In this regime, D_n–κ profiles diverge for cells of varying ζ. A lower velocity ($D_n < D_{CJ}$), decaying blast regime, fully contains decaying cells ($0.5 < \zeta \leq 1$) as well as again some of the central portions of growing cells (as ζ approaches 0.5). In this decaying blast regime, D_n and κ vary spatially across the wave front for each ζ so that each ζ segment is not geometrically cylindrical, but when accumulated, the data for *all* ζ appear to form a line in D_n–κ space. The regime boundary corresponds to the CJ velocity.

The data trend in the lower velocity regime is thus consistent with elements of a cylindrically expanding blast wave. In the limit of completely unsupported (by any reaction zone) cylindrical blast expansion, the velocity-curvature [31] relationship is linear

$$U_s = \frac{\alpha(\gamma)}{2}\sqrt{\frac{E_s}{\rho_0}}\frac{1}{r} \tag{12}$$

where shock velocity $U_s = D_n$, wave radius $r = 1/\kappa$, $\alpha = f(\gamma)$ where γ is the ratio of specific heats, E_s is the blast source energy, and ρ_0 is the initial mixture density. An expanding blast wave travels along a line of decreasing κ, only experiencing a change in slope when E_s is altered.

Strong detonations driven by transverse wave collisions will initially not follow the behavior of Eq. 12 as the detonation is supported through early overdriven expansion by well-coupled, rapid chemical reactions. In this overdriven expansion regime, if the reaction zone is short, the detonation velocity will not be significantly perturbed by curvature-induced flow and will assume $D_n(\kappa)$ profiles with low slopes similar to the ideal curve in Fig. 2 (i.e., κ has to be sufficiently large to generate a significant perturbation to the reaction zone). As the overdriven detonation decays, transverse waves weaken in strength and the reaction zone begins to decouple from the shock. The process causes the wave to assume a steeper positive slope in D_n–κ-space (as shown on Fig. 2 by line segment AB).

Eventually, near local detonation failure, the reaction zone will fully decouple from the shock front. The resulting shock-flame complex may support some low level of energy feedback into the shock, leading to a positive $D_n(\kappa)$ slope that is less than or equivalent to that of an inert, decaying blast

$$D_n/\kappa \leq \frac{\alpha}{2}\sqrt{E_s/\rho_0}\ . \tag{13}$$

Such a trajectory is indicated by on Fig. 2 by line segment BC and in Fig. 23 by the "decaying blast fit" line

$$D_n = 4.89 + 8.69\kappa\,. \tag{14}$$

Note that the correlation of the numeric data to the decaying blast profile occurs both temporally and spatially in Fig. 23, indicating some elements of self-similar flow. The temporal agreement is indicated by the good overlay of wave data from multiple time steps (or varying ζ). The spatial agreement is evidenced by the fact that segments of each time step (or ζ) lie on the blast decay line.

The source energy E_s provides a measure of the energy associated with the wavefront at (and subsequent to) decoupling of the shock and reaction zone. When distributed across the wavefront circumference at the instant of decoupling, this value may provide a measure of the minimum wavefront surface energy necessary to support a coupled shock and reaction as a detonation. Such an estimate may be relevant to detonation initiation energies in the cylindrical geometry [32]. This approach is not pursued further in the present study.

Thus, the D_n–κ profiles of growing cells in Fig. 23 are consistent with the combination of a short reaction zone detonation at the transverse wave Mach stem (feature 1), decaying to a decoupling detonation a short distance behind (feature 2), and finally assuming a fully decoupled blast wave profile at the center of the cell segment (feature 3). These three structures combine to form the characteristic hook-like structure in D_n–κ space. The lack of the reactive, overdriven Mach stem in the decaying cell leaves only the lower velocity portion of this combination (feature 3), which is the decaying blast profile. The demarcation between these two regimes appears to be close the CJ velocity. As all data below the CJ velocity is consistent with an inert expanding blast wave, the present data implies that exceeding this critical velocity is a necessary condition for detonation coupling to be maintained.

This measured evolution extends the understanding of prior efforts [3, 24, 33, 34], whose visualizations have also shown short reaction zones with minimal induction lengths for locally overdriven shocks and very dramatic increases in induction lengths as the local lead shock strength decays. Correlation of these induction lengths with specific burning mechanisms is an ongoing effort [33, 34]. However, to date, no quantitative method has been proposed to evaluate the instantaneous degree of coupling between this late stage reaction and the shock front dynamics in complex experimental or DNS flows. The evaluation of slopes of the D_n–κ trajectories in the present study may provide such a metric.

While clearly visible in the numerical data, the experimental data scatter obscures the presence of any linear decaying blast profile in D_n–κ space. Alternatively, this scatter may instead contain a curved profile as plotted by experimental fits (black dashed line) in Figs. 12 and 13. In highly irregular mixtures, turbulent combustion has been shown to accelerate the post-shock combustion, inducing deflagration at significantly shorter distances behind the shock front than induction length estimates from purely adiabatic shock compression [33, 34]. Such combustion may weakly couple with the shock front and decrease slope of feature 3 in D_n–κ space below that resulting from a fully inert blast. The present numerical results were conducted via an Euler framework and would not accurately model this phenomenon due to the lack of diffusive mixing; Navier-Stokes theory would be required. However, given that turbulent burning has currently only been shown to be as significant feature in highly irregular mixtures, it is likely not a dominant factor in the (regular) weakly unstable mixtures analyzed herein.

5. From D_n–κ Trends to DSD Analysis

In this work, we have studied the variation of the normal detonation shock velocity and shock curvature during the evolution of weakly unstable cellular detonation fronts. These geometric properties have provided insight into the dominant mechanisms (coupled detonation, blast expansion) associated with different parts of the cellular cycle.

We have not attempted to interpret this into an intrinsic unsteady front evolution theory, such as detonation shock dynamics (DSD). Classical DSD theory applies to the quasi-steady evolution of a weakly curved stable detonation; formally asymptotic higher-order corrections which account for (slow) time relaxation effects and small transverse arc-length variations on the evolution of a weakly curved stable detonation have also been developed [14, 22, 23].

The quasi-steady and weak curvatures assumptions that underlie DSD theory have also been applied to the description of unstable cellular detonation dynamics [18]. However, from the work reported here, it is clear that significant rapid time and curvature variations can occur locally during various stages of the cell cycle, and a fully time-dependent non-local front evolution theory may be needed to describe unsteady cellular detonation dynamics in general.

6. Conclusions

This work has characterized the effect of the cellular instability on the lead shock shape and velocity evolution for weakly unstable gaseous detonations. For the first time, variations in local (normal) shock velocity and curvature are reported across the full perimeter of detonation cells. Analysis of quasi-two-dimensional experimental detonation wave fronts demonstrated that, at the cell centerline, the local shock velocity and curvature monotonically decrease throughout the cellular cycle. The range of wavefront curvature present away from the centerline axis was found to be significantly larger for expanding cells as compared to shrinking ones. From this measurement, it was inferred that most curvature variation in a detonation cell occurs downstream of the Mach stem and that shrinking detonation cells assume an approximately cylindrical wavefront profile. However, the experimental analysis was subject to limitations due to data uncertainty and the assumed waveform profile that was fit to each detonation cell segment.

High-resolution direct numerical simulation was also used to study the cellular wavefront evolution using a shock-fit, shock-attached strategy [28, 29], for which geometric properties of the wavefront are generated directly. The calculation both confirmed the experimental observations and characterized the lead shock velocity and curvature variations in significant detail. The lead shock was found to exhibit the highest velocity and curvature spans in the portion of the growing cell immediately downstream to the Mach stem. The curvature extended into negative values (concave facing the direction of bulk wave motion) in this region. Peak values of shock velocity and curvature did not occur at the Mach stem point, but rather a short distance away towards the cell's centerline. Further towards the cell center, the shock exhibited monotonically decreasing local velocity and curvature.

In velocity–curvature space, these behaviors mapped to three distinct features: (feature 1) a small slope, large-curvature-span flat curve for the reactive flow immediately adjacent to the Mach stem, characteristic of the velocity–curvature profile of an explosive with a spatially small reaction zone; (feature 2) a "hook" structure associated with the peak velocity and curvature values; and (feature 3) a large-slope, narrow-curvature-span flat curve characteristic of both a long reaction zone explosive, for which curvature has a significantly greater influence on detonation velocity than small-reaction-zone explosives, and an inert cylindrical decaying blast wave, which has a linear trajectory in velocity–curvature space. Comparison of cells in different stages of evolution showed that, in velocity–curvature space, all low-slope (feature 1) and hook (feature 2) profiles occurred above the Chapman-Jouguet velocity, but did not overlay. Below the Chapman–Jouguet velocity, accumulated large-slope curves (feature 3) traced out a linear D_n–κ curve. Newly developed, growing cells displayed only features 1 and 2. As the growing cells evolved, feature 3 first appeared and subsequently grew in span. As the cell began to shrink due to encroachment of Mach stems from neighboring cells, features 1 and 2 were eliminated from the velocity–curvature profile, leaving only feature 3. The curvature and velocity span of feature 3 decreased with the size of the decaying cell.

The low-slope (feature 1) and hook (feature 2) structures were associated with high and decreasing levels of reaction zone strength and shock coupling. The high-slope (feature 3) region was attributed to a decaying inert shock wave. The data indicates that, for weakly unstable detonation, coupling between the shock and reaction zone only occurs near the Mach stem in growing cells and that the lead shock diffracts in an inert fashion away from this region. Exceeding the Chapman–Jouguet velocity appeared to be a necessary condition for shock and reaction zone coupling to exist in the single computation presented.

7. Acknowledgements

The authors are extremely grateful to J. Austin for providing the film data for this study. We thank S. Lau-Chapdelaine and M. Radulescu for the fitting of one-step rate parameters and T. Aslam for advice on use of the shock-fitting code developed in Ref. [28]. We also acknowledge discussions with J. Kasahara and H. Nakayama on the application of DSD concepts to gas-phase detonation dynamics. This effort was supported through the Campaign 2 "High Explosive Science" and Advanced Scientific Computing (ASC) programs via the Department of Energy.

References

[1] M. Radulescu, J. Lee, The failure mechanism of gaseous detonations: Experiments in porous wall tubes, Combustion and Flame 131 (2003) 29–46.

[2] J. Lee, The Detonation Phenomenon, Cambridge University Press, New York, 2008.

[3] J. Austin, F. Pintgen, J. Shepherd, Reaction zones in highly unstable detonations, in: Proceedings of the 30th International Symposium on Combustion, volume 30, Combustion Institute, Pittsburgh, PA, 2005, pp. 1849–1857.

[4] R. Strehlow, A. Crooker, The structure of marginal detonation waves, Acta Astronautica 1 (1974) 303–315.

[5] D. Edwards, A. Jones, The variation in strength of transverse shocks in detonation waves, J. Phys. D: Appl. Phys. 11 (1978) 155–166.

[6] E. A. Lundstrom, A. K. Oppenheim, On the influence of non-steadiness on the thickness of the detonation wave, Proc. R. Soc. A 310 (1969) 463–478.

[7] M. Dormal, J.-C. Libuton, P. V. Tiggelen, Evolution of induction time in detonation cells, Acta Astronautica 6 (1979) 875–884.

[8] H. Jones, A theory of the dependence of the rate of detonation of solid explosives on the diameter of the charge, Proc. Royal Soc., Series A 1018 (1947) 415–426.

[9] H. Eyring, R. P. G. Duffey, R. Parlin, The stability of detonation, Chem. Rev. 45 (1949) 69–181.

[10] W. Wood, J. Kirkwood, Diameter effect in condensed explosives. the relation between velocity and radius of curvature of the detonation wave, Journal of Chemical Physics 22 (1954) 1920–1924.

[11] J. Bdzil, Steady-state two-dimensional detonation, Journal of Fluid Mechanics 108 (1981) 195–226.

[12] J. B. Bdzil, W. Fickett, D. S. Stewart, Detonation shock dynamics: A new approach to modeling multi- dimensional detonation waves, in: Ninth Symposium (Int.) on Detonation, Office of Naval Research, 1989, pp. 730–742.

[13] J. Bdzil, D. Stewart, The dynamics of detonation in explosive systems, Ann. Rev. Fluid Mech. 39 (2007) 263–292.

[14] J. Bdzil, T. Aslam, M. Short, DSD front models: Nonideal explosive detonation in ANFO, in: Twelfth Symposium (Int.) on Detonation, pp. 409–417.

[15] C. Eckett, J. Quirk, J. Shepherd, The role of unsteadiness in direct initiation of gaseous detonations, Journal of Fluid Mechanics 421 (2000) 147–183.

[16] M. Short, G. Sharpe, Direct initiation of three-step chain-branching reaction detonation, 2013. In Preparation.

[17] L. He, P. Calvin, On the direct initiation of gaseous detonations by an energy source, Journal of Fluid Mechanics 277 (1994) 227–248.

[18] D. Stewart, T. Aslam, J. Yao, On the evolution of cellular detonation, in: Proceedings of the 26th International Symposium on Combustion, volume 26, Combustion Institute, Pittsburgh, PA, 1996, pp. 2981–2989.

[19] J. Yao, D. Stewart, On the normal detonation shock velocity–curvature relationship for materials with large activation energy, Combustion and Flame 100 (1995) 519–528.

[20] R. Klein, J. Krok, J. Shepherd, Curved Quasi-Steady Detonations: Asymptotic Analysis and Detailed Chemical Kinetics, Technical Report FM95-04, Graduate Aeronautical Laboratories, California Institute of Technology, Pasadena, CA, 1996.

[21] H. Nakayama, T. Moriya, J. Kasahara, A. Matsuo, Y. Sasamoto, I. Funaki, Stable detonation wave propagation in rectangular-cross-section curved channels, Combustion and Flame doi:10.1016/j.combustflame.2011.07.022 (2011).

[22] R. Klein, On the dynamics of weakly curved detonations, IMA-Volumes in Mathematics and its Applications 35 (1991).

[23] J. Bdzil, M. Short, G. Sharpe, T. Aslam, J. Quirk, Higher-order dsd for detonation propagation: Dsd for detonation driven my multi-step chemistry models with disparate rates, in: 13th Symposium (Int.) on Detonation, Office of Naval Research, 2006, pp. 726–736.

[24] J. Austin, The Role of Instability in Gaseous Detonation, Ph.D. thesis, California Institute of Technology, 2003.

[25] R. Catanach, L. Hill, Diameter effect curve and detonation front curvature measurements for ANFO, in: Shock Compression of Condensed Matter, American Institute of Physics, 2001, pp. 906–909.

[26] G. Sharpe, J. Quirk, Nonlinear cellular dynamics of the idealized detonation model: Regular cells, Combustion Theory and Modeling 12 (2007) 1–21.

[27] J. Li, Z. Zhao, A. Kazakov, F. L. Dryer, An updated comprehensive kinetic model of hydrogen combustion, Int. J. Chem. Kinet. 36 (2004) 566–574.

[28] A. Henrick, Shock-fitted numerical solutions of one- and two-dimensional detonation, Ph.D. thesis, University of Notre Dame, 2008.

[29] A. Henrick, T. Aslam, J. Powers, Simulations of pulsating one-dimensional detonations with true fifth order accuracy, J. Computat. Phys. 213 (2006) 311–329.

[30] M. Short, I. Anguelova, T. Aslam, J. Bdzil, A. Henrick, G. Sharpe, Stability of detonations for an idealized condensed-phase model, Fluid Mechanics 595 (2008) 1–21.

[31] L. Sedov, Similarity, modeling and various examples of dimensional theory, in: Similarity and Dimensional Methods in Mechanics, Tenth Edition, CRC, 1993, pp. 37–116.

[32] M. Radulescu, A. Higgins, S. Murray, J. Lee, An experimental investigation of the direct initiation of cylindrical detonations, Journal of Fluid Mechanics 480 (2003) 1–24.

[33] M. Radulescu, G. Sharpe, C. Law, J. Lee, The hydrodynamic structure of unstable cellular detonations, Journal of Fluid Mechanics 580 (2007) 31–38.

[34] C. Kiyanda, A. Higgins, Photographic investigation into the mechanism of combustion in irregular detonation waves, Shock Waves (2012).

8. Figures

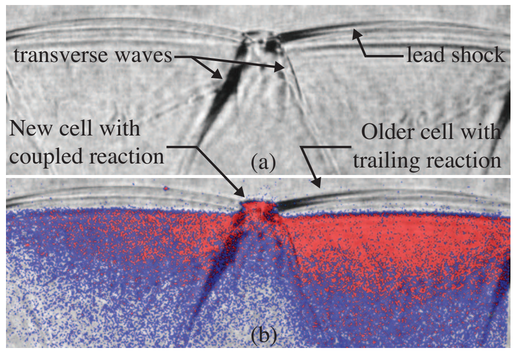

Figure 1: Schlieren image of detonation from Austin [24] showing (a) Mach stem creation from transverse wave collision and (b) a color intensity overlay of the OH reaction-zone species (red-to-blue signifies high-to-low intensity). Wave propagation direction is up.

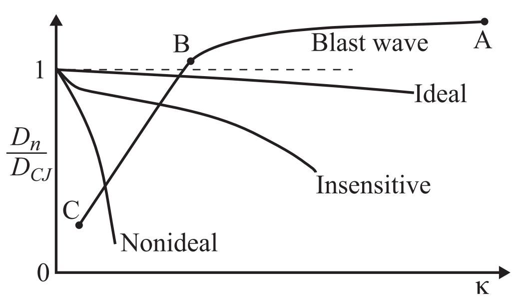

Figure 2: D_n–κ trends.

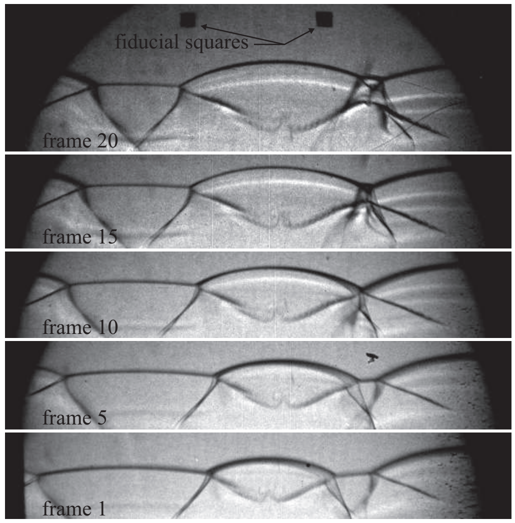

Figure 3: Multiple shadowgraph frames from test NC260 in Austin [24]. Wave propagation direction is up.

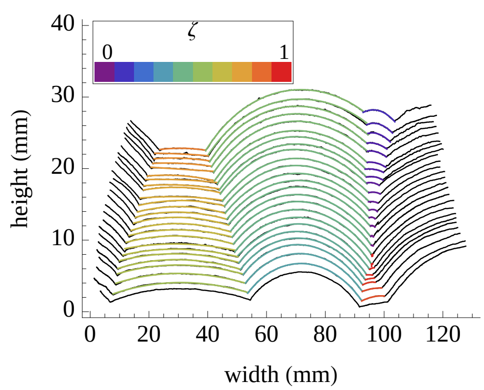

Figure 4: Processed front data from test NC260 in Austin [24]. Wave propagation direction is up.

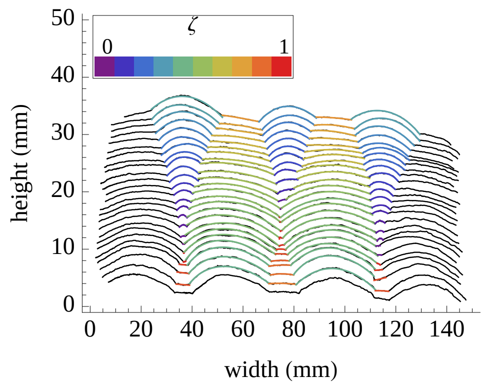

Figure 5: Processed front data from test NC229 in Austin [24]. Wave propagation direction is up.

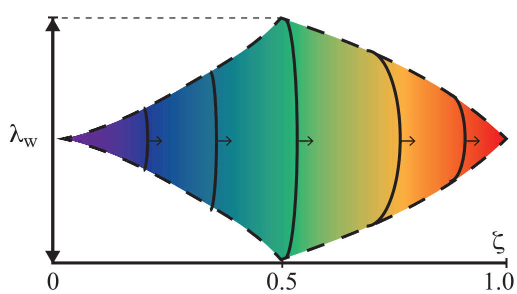

Figure 6: A graphical description of ζ. Dashed lines denote triple point tracks; solid curves are the detonation shock sketched at different timesteps.

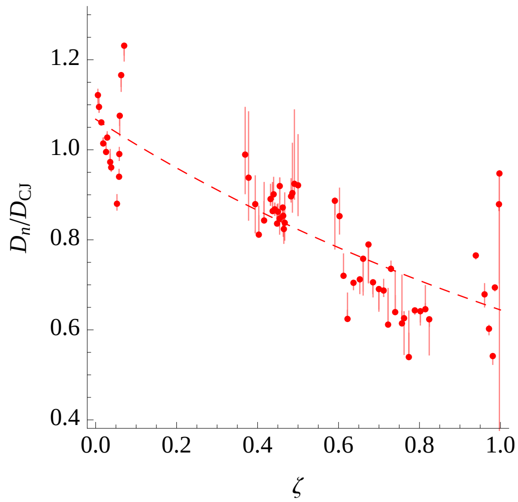

Figure 7: D_n variation with ζ for NC260.

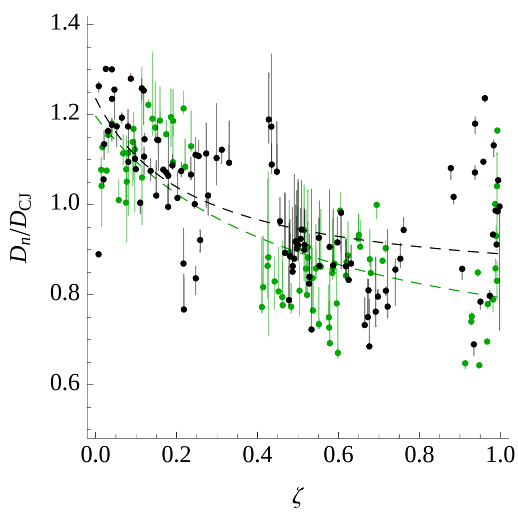

Figure 8: D_n variation with ζ for NC215 (green) and NC229 (black).

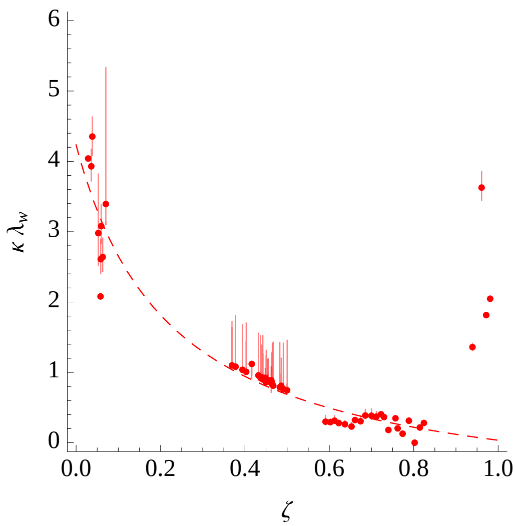

Figure 9: κ variation with ζ for NC260.

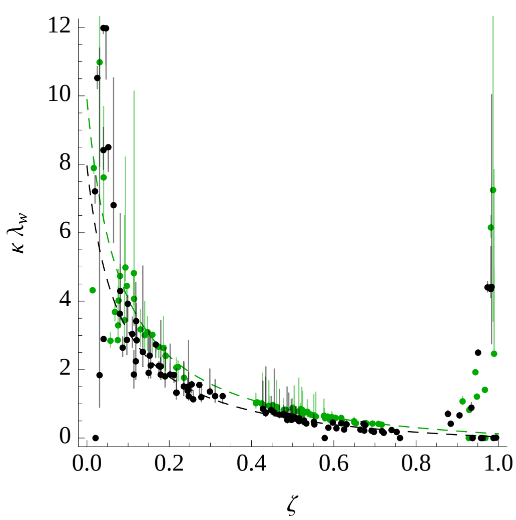

Figure 10: κ variation with ζ for NC215 (green) and NC229 (black).

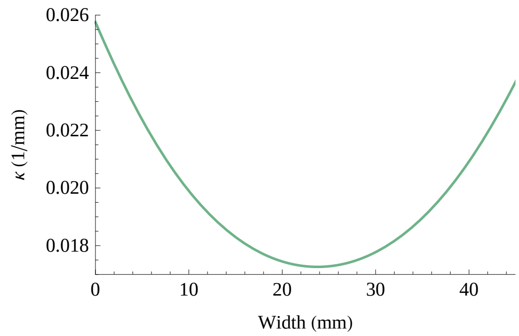

Figure 11: κ versus channel width for a wave segment with $\zeta = 0.44$ from NC260.

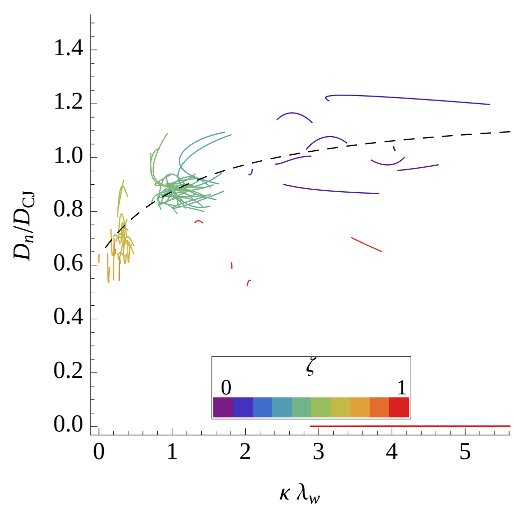

Figure 12: D_n–κ relationships for NC260 from Fig. 4.

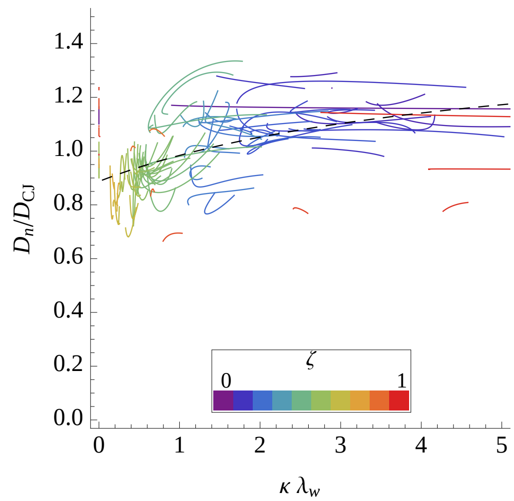

Figure 13: D_n–κ relationships for NC229 from Fig. 5.

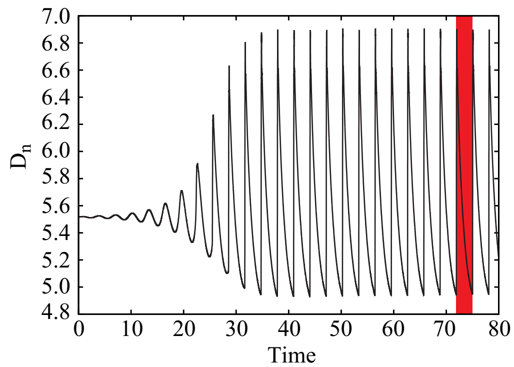

Figure 14: Variation of D_n along the channel centerline with time for the 80% Ar mixture. The red shaded region indicates the time region from which all successive figures are drawn.

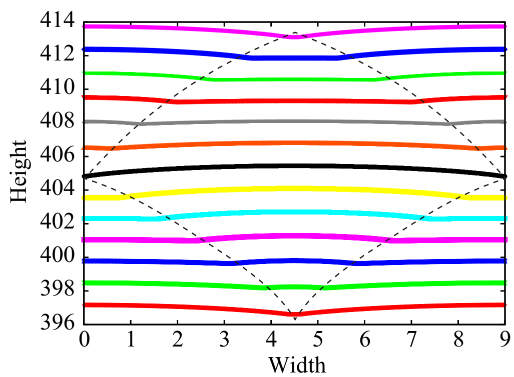

Figure 15: Position of the shock loci (over one cell duration) as a function of channel height and width (start time $t = 72$, end time $t = 75$, with time intervals of 0.25) for the 80% Ar mixture.

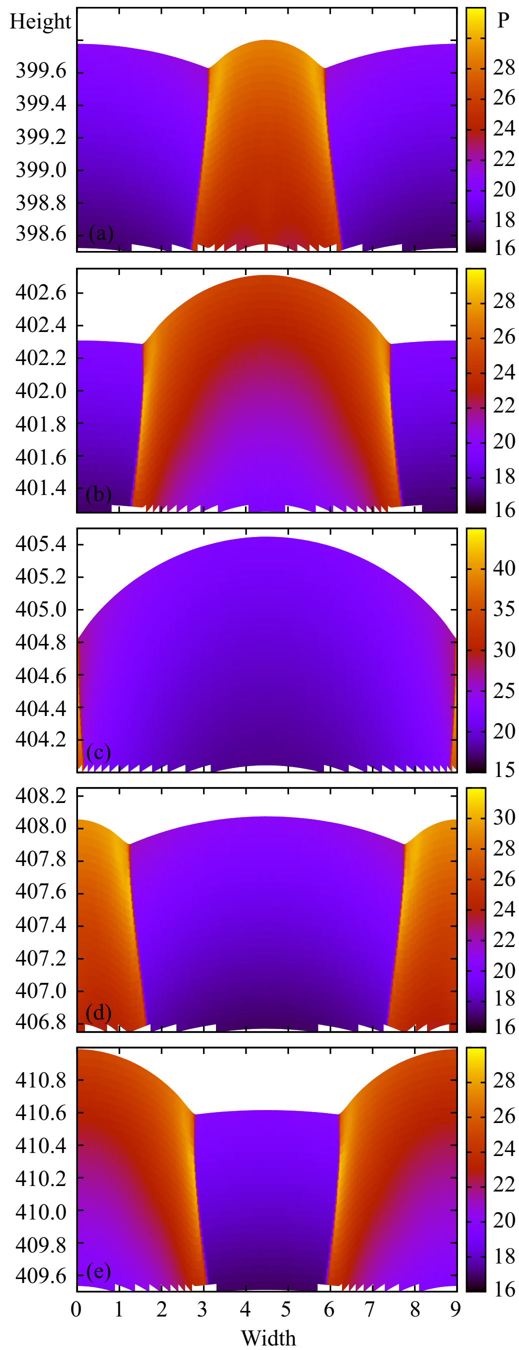

Figure 16: Snapshots of the numerically calculated cell pressure distribution in the 80%Ar mixture for (a) $t = 72.5$, (b) $t = 73$, (c) $t = 73.5$, (d) $t = 74$, and (e) $t = 74.5$.

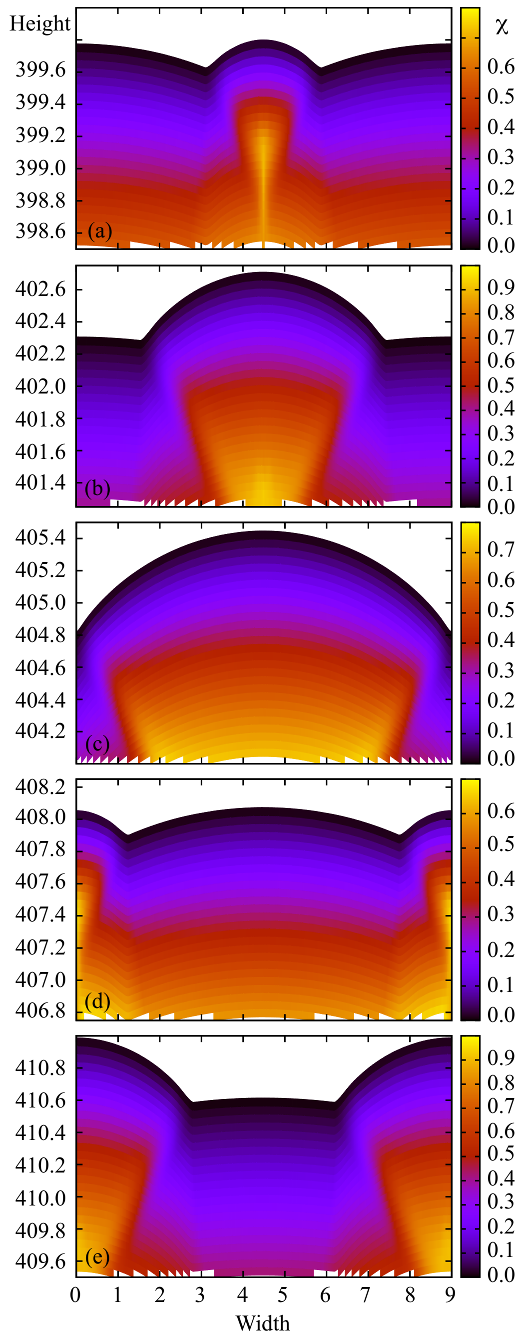

Figure 17: Corresponding snapshots of the numerically calculated cell reaction progress variable distribution in the 80%Ar mixture for the times shown in Fig. 16.

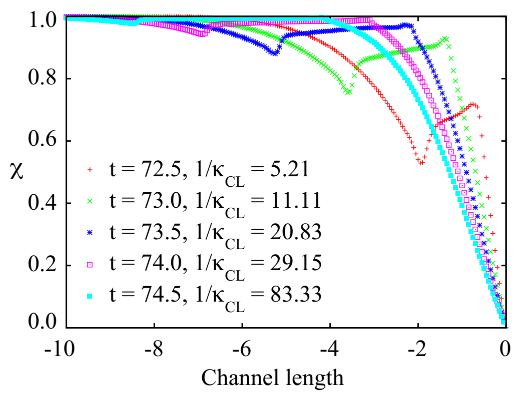

Figure 18: Axial variation of reaction progress variable χ along the channel center $y = 4.5$ at $t = 72.5$ (red), $t = 73$ (green), $t = 73.5$ (blue), $t = 74$ (pink) and $t = 74.5$ (turquoise).

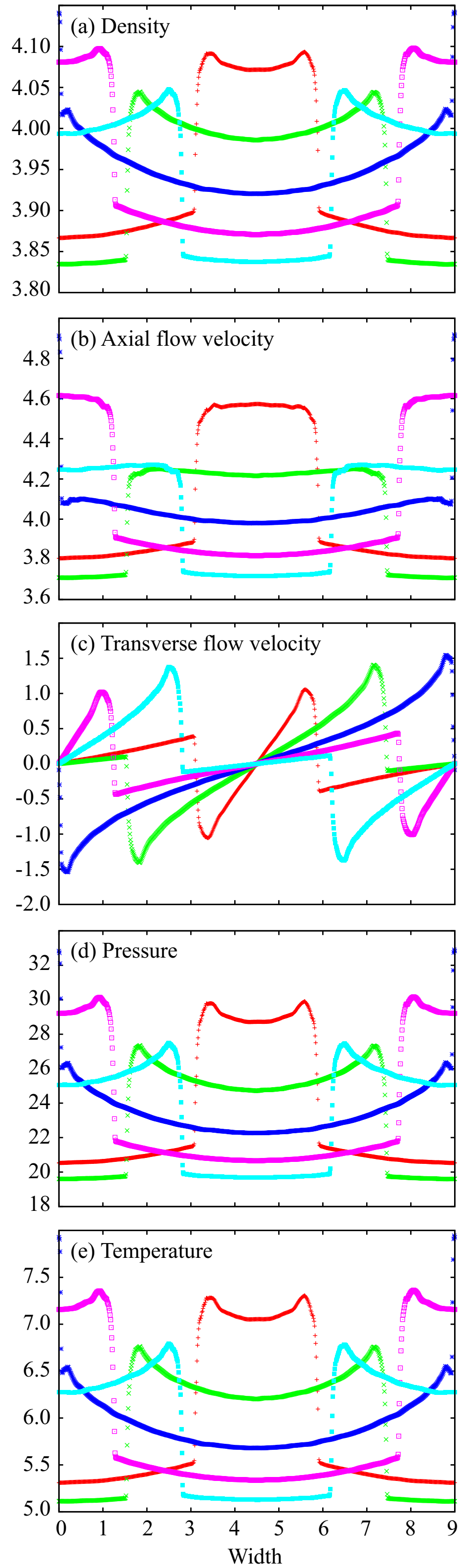

Figure 19: Numerically calculated distributions of (a) density, (b) axial velocity, (c) transverse velocity, (d) pressure and (e) temperature along the lead shock front at times $t = 72.5$ (red), $t = 73$ (green), $t = 73.5$ (blue), $t = 74$ (pink) and $t = 74.5$ (turquoise).

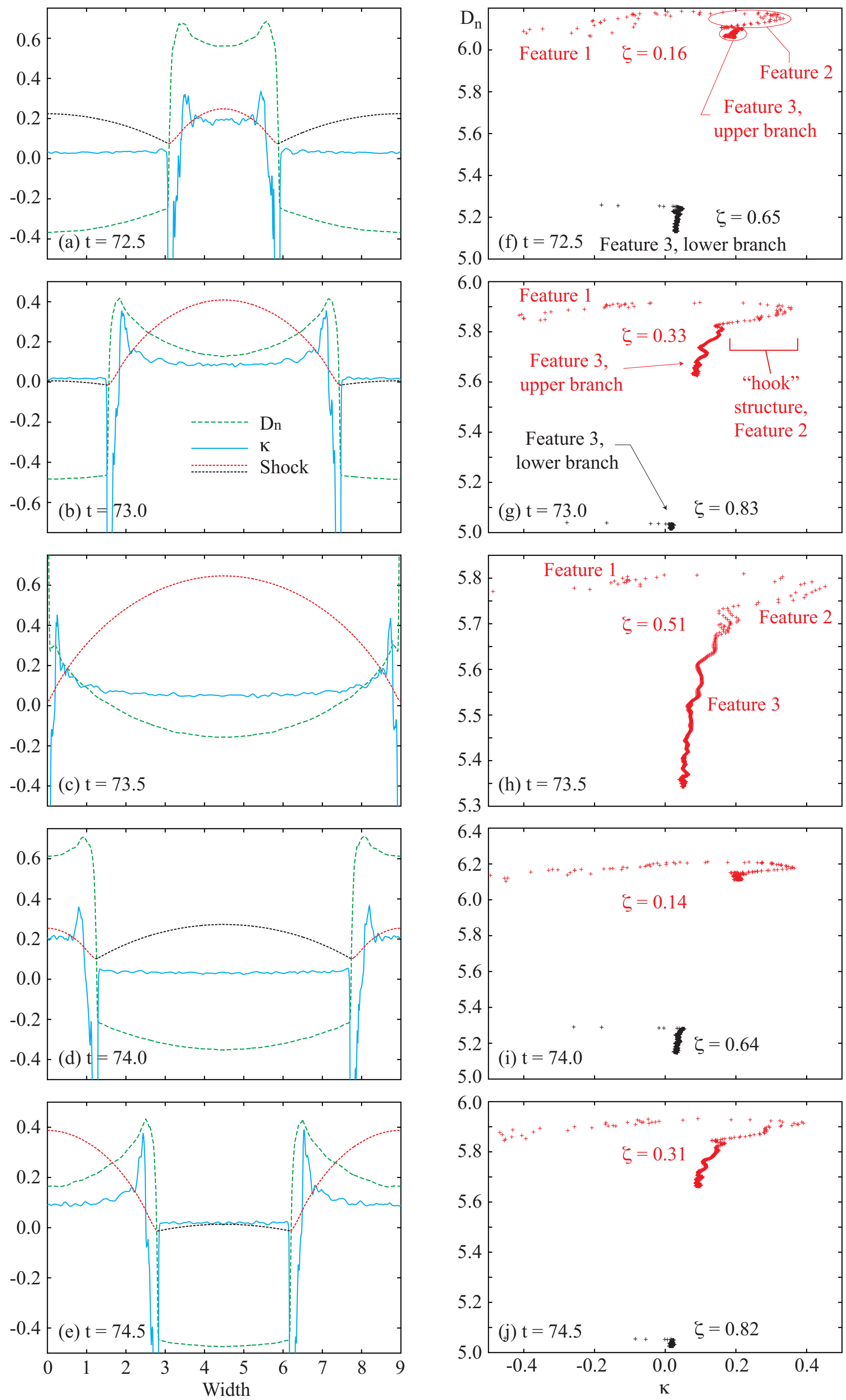

Figure 20: Variation of D_n (green curves) and κ (blue curves) along the growing (red) and decaying (black) shock loci for the 80% Ar mixture for five timesteps. For (a)–(e), plotted D_n values are relative to 5.5, while shock loci have been displaced by (a) -399.5, (b) -402.3, (c) -404.8, (d) -407.8 and (e) -410.6. Plots (f)–(j) show the variation of D_n with κ for each corresponding shock segment from plots (a)–(e).

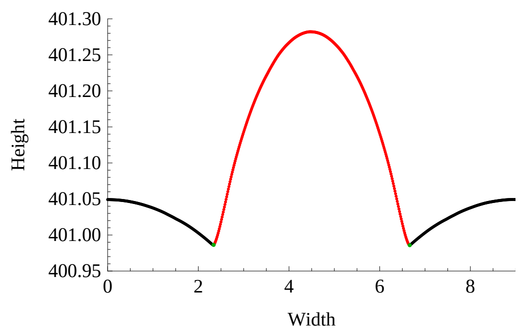

Figure 21: The computed shock shape at $t = 72.75$.

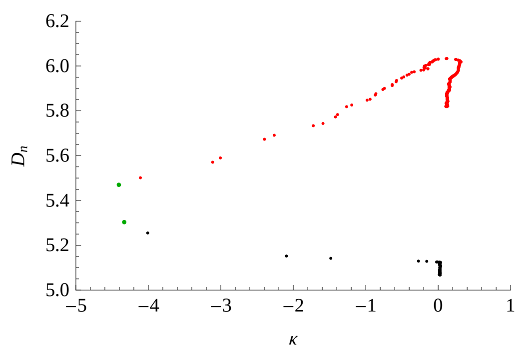

Figure 22: D_n and κ values from the computed shock shape in Fig. 21.

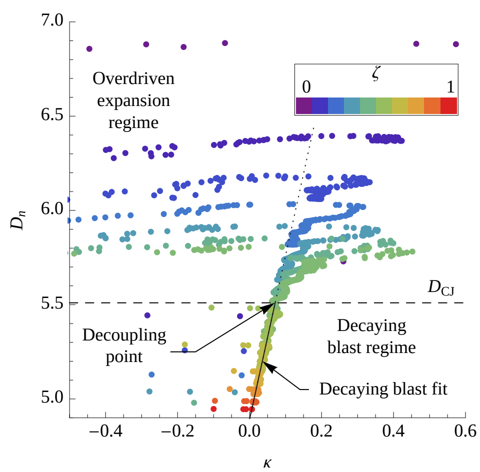

Figure 23: Variation of D_n with κ for multiple values of ζ.